

# When Will MISR Detect Rising High Clouds?

Travis Aeronson<sup>1</sup>, Roger Marchand<sup>1</sup>, H el ene Chepfer<sup>2</sup>, and Brian Medeiros<sup>3</sup>

<sup>1</sup>University of Washington

<sup>2</sup>LMD/IPSL Sorbonne Universit e

<sup>3</sup>National Center for Atmospheric Research

November 30, 2022

## Abstract

It is predicted by both theory and models that high clouds will occur higher in the atmosphere as a result of climate warming. This change produces a positive longwave feedback and has a substantial impact on the Earth's response to warming. This effect is well established by theory, but is poorly constrained by observations, and there is large spread in the feedback strength between climate models. We use the NASA Multi-angle Imaging SpectroRadiometer (MISR) to examine changes in Cloud-Top-Height (CTH). MISR uses a stereo-imaging technique to determine CTH. This approach is geometric in nature and insensitive to instrument calibration and therefore is well suited for trend analysis and studies of variability on long time scales. In this article we show that the current MISR record does have an increase in CTH for high-altitude cloud over the Southern Hemisphere (SH) but not over the Tropics or the Northern Hemisphere (NH). We use climate model simulations to estimate when MISR might be expected to detect a global trend in CTH, that would include the NH. The analysis suggests that according to the models used in this study MISR should detect changes over the SH ocean earlier than the NH, and should be capable of detecting a trend over the Tropics and NH very soon (3 to 10 years). This result highlights the potential value of a follow-on mission to MISR, which no longer maintains a fixed equator crossing time and is unlikely to be making observations for another 10 years.

## Hosted file

aeronson\_etal\_2021\_misr\_cth\_trends\_supplement\_submission.docx available at <https://authorea.com/users/560048/articles/608284-when-will-misr-detect-rising-high-clouds>

1  
2  
3  
4  
5  
6  
7  
8  
9  
10  
11  
12  
13  
14  
15  
16  
17  
18

## When Will MISR Detect Rising High Clouds?

Travis Aeronson<sup>1</sup>, Roger Marchand<sup>1</sup>, H el ene Chepfer<sup>2</sup>, and Brian Medeiros<sup>3</sup>

<sup>1</sup>University of Washington, Department of Atmospheric Sciences

<sup>2</sup>LMD/IPSL, Sorbonne Universit e

<sup>3</sup>National Center for Atmospheric Research, Climate and Global Dynamics

Corresponding author: Travis Aeronson (aeronson@uw.edu)

### Key Points:

- The current MISR observational record shows an increase in cloud-top-height (CTH) of high cloud over the Southern Hemisphere Oceans.
- Climate models suggest that rising CTH due to climate warming should be globally observable in the near future.
- Models with higher ECS have more rapidly rising high-clouds, but this does not always lead to an earlier observable trend.

**19 Abstract**

20 It is predicted by both theory and models that high clouds will occur higher in the atmosphere as  
21 a result of climate warming. This change produces a positive longwave feedback and has a  
22 substantial impact on the Earth's response to warming. This effect is well established by theory,  
23 but is poorly constrained by observations, and there is large spread in the feedback strength  
24 between climate models. We use the NASA Multi-angle Imaging SpectroRadiometer (MISR) to  
25 examine changes in Cloud-Top-Height (CTH). MISR uses a stereo-imaging technique to  
26 determine CTH. This approach is geometric in nature and insensitive to instrument calibration  
27 and therefore is well suited for trend analysis and studies of variability on long time scales. In  
28 this article we show that the current MISR record does have an increase in CTH for high-altitude  
29 cloud over the Southern Hemisphere (SH) but not over the Tropics or the Northern Hemisphere  
30 (NH). We use climate model simulations to estimate when MISR might be expected to detect a  
31 global trend in CTH, that would include the NH. The analysis suggests that according to the  
32 models used in this study MISR should detect changes over the SH ocean earlier than the NH,  
33 and should be capable of detecting a trend over the Tropics and NH very soon (3 to 10 years).  
34 This result highlights the potential value of a follow-on mission to MISR, which no longer  
35 maintains a fixed equator crossing time and is unlikely to be making observations for another 10  
36 years.

**37 Plain Language Summary**

38 There is a feedback to climate change associated with high-altitude clouds rising higher up in the  
39 atmosphere that is predicted by physical theory to enhance warming, and is found in a wide  
40 range of models. To date, there is little observational evidence for rising high clouds. An  
41 observation of a trend in cloud-top-height (CTH) in the atmosphere would enhance our  
42 understanding of this feedback, and climate warming as a whole. This study uses the Multi-angle  
43 Imaging SpectroRadiometer (MISR) to examine changes in CTH. Currently the MISR  
44 observational record does show a trend in CTH in the Southern Hemisphere (SH) oceans, but  
45 does not show a trend over the Tropics or the Northern Hemisphere (NH) oceans. We use model  
46 simulations to examine how long it should take for MISR to observe trend changes in CTH that  
47 include the Tropics and NH. The models used in this study suggest that MISR should be capable  
48 of observing a trend in the next 3 to 10 years. MISR is unlikely to be making measurements  
49 suitable for this kind of trend analysis for another 10 years, and this highlights the value of a  
50 follow-on mission to MISR which can extend the stereo-imaging record.  
51

## 52 **1. Introduction**

53 Clouds play an important role in the Earth radiation budget. They simultaneously cool the  
54 Earth by reflecting shortwave sunlight, and insulate the Earth by reducing longwave emission to  
55 space. Cloud feedbacks (how clouds change in response to forcing) are important to  
56 understanding the future of climate (Schneider, 1972; Stephens, 2005; Webb et al., 2017), and  
57 yet are one of the largest causes of uncertainty (spread) in climate model projections (Soden &  
58 Held, 2006; Zelinka et al., 2020). The amplitudes and sign of many cloud feedbacks vary among  
59 climate models. One cloud feedback on which there is broad agreement, however, is that the  
60 cloud-top-height (CTH) of high clouds at all latitudes will experience an upward shift in altitude  
61 as the surface and troposphere warm. An increase in CTH with warming has been seen in climate  
62 simulations dating back to the 1980s (Hansen, 1984; Wetherald & Manabe, 1988), and remains a  
63 robust feature in modern cloud resolving models and climate model simulations (Harrop &  
64 Hartmann, 2012; Kuang & Hartmann, 2007; Zelinka et al., 2013).

65 This effect is a well understood response to warming, explained by the Fixed Anvil  
66 Temperature (FAT) hypothesis: which asserts that the height at which high altitude anvil clouds  
67 form is nearly fixed in temperature and is independent of surface temperature (Hartmann &  
68 Larson, 2002; Zelinka & Hartmann, 2010). Anvil temperature is nearly fixed because anvils form  
69 where latent heating by condensation balance clear sky longwave radiative cooling. The vertical  
70 profile of clear-sky longwave cooling is largely controlled by the vertical distribution of water  
71 vapor. The Clausius-Clapeyron equation shows that, assuming the atmosphere is near saturation  
72 (which on large scales is typically a good approximation), the water vapor content decreases  
73 quasi-exponentially with temperature. Consequently, at sufficiently cold temperatures, there is  
74 insufficient water vapor to significantly cool the atmosphere through thermal emission to space  
75 (as compared with the warmer and moister atmosphere below) and the rapid decrease in water  
76 vapor effectively sets a preferential temperature for the top of the longwave cooling profile (and  
77 consequently anvil cloud formation). A slightly altered version of the FAT hypothesis was  
78 developed by Zelinka & Hartmann (2010), which asserts that the preferential temperature for  
79 anvil tops will warm slightly (are not truly fixed) because there will be larger static stability in  
80 the upper atmosphere. Which results in anvil clouds rising in the atmosphere, but at a slower rate  
81 than required to remain at a constant temperature. We note the spectroscopy of water vapor (the  
82 change in opacity of water vapor with frequency and pressure that arises from the quantum  
83 mechanical properties of water vapor molecules) play a critical role in the radiative cooling  
84 profile. Cooling is not restricted to a narrow band near the top of the water-vapor profile, but  
85 cooling is distributed throughout the depth of the troposphere and helps set this critical  
86 temperature where the longwave cooling “kinks” at around 220 K (Jeevanjee & Fueglistaler,  
87 2020).

88 Rising CTH with a fixed anvil temperature creates a positive feedback on climate, because  
89 while the surface warms and longwave emission to space increases from the surface, the  
90 emission temperature of anvil cloud changes very little. So, more heat is held by the Earth  
91 system than if anvil temperatures warmed proportionally to the surface temperature. Of course,  
92 reduction in high cloud area or thickness (opacity to infrared) could offset the change in CTH,  
93 and this possibility remains a topic of considerable interest (Bony et al., 2016). Nonetheless,  
94 rising CTH creates a positive longwave feedback. We also note that while the FAT hypothesis  
95 was originally developed for tropical anvil clouds, changes in the clear-sky radiative cooling  
96 profiles are likewise expected in midlatitudes, and the theory that anvil cloud height follows the

97 clear-sky radiative cooling profile appears to hold well in the midlatitudes (Thompson et al.,  
98 2017).

99 Interestingly, there has been evidence that the tropopause may increase in altitude in a way  
100 that is fixed in temperature (Seeley et al., 2019). It has long been understood that the tropopause  
101 (and associated thin clouds) will increase in height with climate change (Hu & Vallis, 2019;  
102 Vallis et al., 2015; Zhou et al., 2014), but it is a relatively new result that the tropopause may be  
103 tightly linked to the temperature profile. Seeley et al. (2019) identified this behavior based on  
104 model simulations, and the physical mechanisms are yet to be established.

105 Regardless of the physical mechanisms responsible for rising CTH, the associated LW  
106 feedback is produced consistently in models, but it's contribution to the global energy budget  
107 varies from model to model. Thus, it is important to study and understand this positive feedback  
108 mechanism. Satellites provide a particularly advantageous position for observing cloud-top, and  
109 satellite measurements could potentially be used to evaluate or constrain model simulations of  
110 cloud-top-height.

111 To date there is little evidence in the observational record for increasing cloud-top-height of  
112 high cloud. Norris et al. (2016) (hereafter N16) used the International Satellite Cloud  
113 Climatology Project (ISCCP) and Extended Pathfinder Atmospheres (PATMOS) infrared  
114 satellite records to examine how zonally averaged cloud profiles have changed between the  
115 decades of the 1980s and the 2000s. N16 found that the ISCCP and PATMOS zonal mean cloud  
116 amounts increased in the 50-180 hPa interval and decreased in the 180-310 interval during the  
117 period 1983-2009 in the tropics, which is consistent with a rise in the tops of the highest clouds.  
118 However, no estimate of the rate of CTH increase was made. Further, the reliability of the  
119 ISCCP/PATMOS satellite record is a concern, as the ISCCP/PATMOS record uses many  
120 satellites/sensors whose number and position have changed over time, and in general are not  
121 calibrated consistently. The infrared retrieval technique for CTH is sensitive to changes in cloud  
122 emissivity, view angles, and calibration (Rossow et al., 1993). Consequently, there remains a  
123 strong need to understand and quantify CTH trends.

124 There have been a small number of studies which use satellite simulators embedded into  
125 climate models to determine when we will be capable of constraining the rate of rising CTH (and  
126 thus the associated feedback) (Chepfer et al., 2018; Chepfer et al., 2014; Takahashi et al., 2019).  
127 Two such studies, Chepfer et al. (2018, 2014) (hereafter C18, and C14) made use of a Calipso  
128 (spaceborne lidar) simulator in AMIP (Atmospheric Model Intercomparison Project) and  
129 AMIP+4K simulations to estimate how long of a Calipso record might be required to observe  
130 trends in CTH. C14 focused on tropical high clouds (but also looked at other regions), and used a  
131 linear assumption of global warming from the current temperatures, to a +4K world. They found  
132 that the Calipso record would need to be 15-30 years past the start of the model simulation  
133 (2008) to detect a climate trend. C18 used similar methods to C14. Based on output from two  
134 climate models they found that a 27-year data record would be needed to distinguish differences  
135 in the rate of change in CTH between the two models with 70% confidence.

136 Takahashi et al., (2019) (hereafter T19) used a fully coupled simulation from CESM1  
137 (Community Earth System Model version 1) running the Representative Concentration Pathway  
138 8.5 scenario with 8.5 W/m<sup>2</sup> of radiative forcing at 2100 (RCP 8.5), to determine when CloudSat  
139 (or a similar spaceborne radar) would be capable of observing a climate trend in CTH. This  
140 simulation included output from the COSP Quickbeam radar simulator (Bodas-Salcedo et al.,  
141 2011). They forecast that the earliest possible time for a confident (95%) detection based on  
142 CloudSat would be in 2028.

143 Here we undertake a similar analysis to T19 to determine when rising CTH will be detectable  
144 with high confidence, but focus on detectability based on CTH from a stereo-imaging technique,  
145 which follows that used by the Multi-angle Imaging Spectroradiometer (MISR) instrument  
146 (Marchand et al., 2007). In doing so we make extensive use of MISR simulator output  
147 (Marchand & Ackerman, 2010; Swales et al., 2018). The stereo-imaging technique employed by  
148 MISR uses nine cameras to collect images of the Earth from nine different view angles as the  
149 satellite moves along a sun synchronous orbit (Diner et al., 1998). MISR determines cloud-top-  
150 height (CTH) using stereo-image parallax, a geometric calculation which is independent of  
151 image calibration (Marchand & Ackerman, 2010; Marchand et al., 2007; Moroney et al., 2002).

152 MISR CTH retrievals have been compared to heights obtained from ground-based and  
153 spaceborne radar and lidar and were found to produce very reliable cloud-top-height  
154 measurements for cloud with optical depth greater than 0.3 (Hillman et al., 2017; Marchand et  
155 al., 2007). Knowing this, and that MISR has a relatively long continuous data record (roughly 20  
156 years), it is clear that MISR is a good candidate for detecting and quantifying any climate trend  
157 in CTH.

158 Our analysis is largely based on output from two climate models running the fifth Shared  
159 Socio-economic Pathway with  $8.5 \text{ W/m}^2$  of forcing at 2100 (SSP 585) simulation, specifically  
160 we use output from the Community Earth System Model version 2 (CESM2) and the latest  
161 climate model from Institute Pierre-Simon Laplace (IPSL-CM6A-LR). We also extrapolate  
162 results based on a larger collection of models that have run the MISR simulator in AMIP  
163 simulations, which are simulations performed using atmospheric models with prescribed the sea-  
164 surface temperature (SST) to match with the historical record. Synthetic climate warming  
165 projections are made using the SSP 585 scenario temperature outputs and AMIP MISR simulator  
166 profiles, assuming the MISR CTH will increase at a rate following the FAT hypothesis.

167 In this article, the data and methods used for the CTH trend emergence analysis are described  
168 in Section 2, which is followed in Section 3 by the time of emergence results for CESM2 and  
169 IPSL-CM6A-LR. Section 4 is dedicated to determining how the rising CTH in these models  
170 compares to a rate that would be predicted by the FAT hypothesis, after which in Section 5 we  
171 use the FAT hypothesis to synthesize how a larger multi-model ensemble might behave, and how  
172 CTH trend emergence is different in models with different warming rates. Finally, Section 6  
173 summarizes results and presents the main conclusions.

174

## 175 **2. Data and Methods**

176

177 This project uses the MISR joint-histogram product, which contains histograms of cloud  
178 occurrence by optical depth and height (Marchand et al., 2010). As was found by Marchand  
179 (2013), and as will be shown later, examination of the MISR cloud-top-height optical depth  
180 (CTH-OD) dataset does not reveal any trends in globally averaged or tropical CTH. This is not a  
181 surprise, because as will be shown later, the size of the expected change in CTH to date is small  
182 relative to internal variability, and a primary objective of our analysis is to determine when  
183 model predicted changes could be detected with high confidence. The MISR simulator, hereafter  
184 referred to as MISR-COSP (because it is part of the Cloud feedback model intercomparison  
185 project Observation Simulator Package (COSP) that is being run by many modeling centers) is  
186 used to produce a MISR-like cloud field that is consistent with the treatment of radiation in each  
187 model (Swales et al., 2018). Details on the MISR simulator can be found in Marchand et al.  
188 (2010) and Marchand & Ackerman (2010) with evaluation of both MISR observations and

189 MISR-COSP output against CloudSat and Calipso (radar and lidar) given by Hillman et al.  
190 (2017).

191 We examine trend detectability in the context of model simulations based on the fifth Shared  
192 Socioeconomic Pathway scenario with  $8.5 \text{ W/m}^2$  of radiative forcing (SSP 585) (O'Neill et al.,  
193 2016). In this simulation  $\text{CO}_2$  and aerosol emissions are set based on observations from 1850 to  
194 2015 before being allowed to increase. The increase in emissions represents a future with  
195 unmitigated emissions, and the implications of this are discussed in the concluding material. As  
196 part of the Coupled Model Intercomparison Project phase 6 (CMIP6), two modeling centers  
197 produced MISR-COSP outputs for SSP 585 simulations, specifically, data is available from the  
198 CESM2 and IPSL-CM6A-LR models. Hereafter the IPSL-CM6A-LR model simulation will be  
199 identified as simply IPSL. The SSP 585 simulation is initialized from the historical run. Thus, we  
200 concatenate the SSP 585 simulation output onto the historical simulation output to create model  
201 time series that begin in 2000 and continue past 2015 and into the future based on projected  
202 emissions.

203 In addition, several models have run the MISR-COSP simulator as a part of the Atmospheric  
204 Model Intercomparison Project (AMIP), which are atmosphere only model simulations that have  
205 sea-surface temperatures prescribed to closely match the historical temperatures from 1979 to the  
206 near present (Gates et al., 1999), but did not generate MISR-COSP output for their SSP 585  
207 simulations. In the analysis we use the MISR-COSP output from the AMIP run in conjunction  
208 with the SSP 585 simulated temperature and geopotential profiles to examine CTH detection  
209 under the assumption of a FAT-like increase in CTH in these models. Specifically, synthetic  
210 MISR projections are produced for CESM2 and IPSL (for comparison with direct MISR  
211 simulator output), as well as MRI-ESM2-0, CanESM5, CNRM-CM6-1, CNRM-ESM2-1, and  
212 BCC-CSM2-MR. Primary references for each of these models is given in **Table 1**. In the  
213 following analysis, these data are first deseasonalized (by subtracting the mean seasonal cycle  
214 from the full length of each dataset), unless stated otherwise.

215  
216

<b>Model</b>	<b>Simulations used</b>	<b>Reference</b>
<b>CESM2</b>	Historical, (MISR-COSP, ta, zg) SSP 585, (MISR-COSP, ta, zg) AMIP (MISR-COSP, ta, zg)	Danabasoglu et al. (2020)
<b>IPSL-CM6A-LR</b>	Historical, (MISR-COSP, ta, zg) SSP 585, (MISR-COSP, ta, zg) AMIP (MISR-COSP, ta, zg)	Boucher et al. (2020)
<b>BCC-CSM2-MR</b>	Historical (ta, zg), SSP 585 (ta, zg), AMIP (MISR-COSP, ta, zg)	Wu et al. (2019)
<b>CanESM5</b>	Historical (ta, zg), SSP 585 (ta, zg), AMIP (MISR-COSP, ta, zg)	Swart et al. (2019)
<b>CNRM-CM6-1</b>	Historical (ta, zg), SSP 585 (ta, zg), AMIP (MISR-COSP, ta, zg)	Voldoire et al. (2019)
<b>CNRM-ESM2-1</b>	Historical (ta, zg), SSP 585 (ta, zg),	S��ferian et al. (2019)

	AMIP (MISR-COSP, ta, zg)	
<b>MRI-ESM2-0</b>	Historical (ta, zg), SSP 585 (ta, zg), AMIP (MISR-COSP, ta, zg)	Yukimoto et al. (2019)

217 *Table 1* A summary of the models used in this analysis. MISR-COSP indicates the simulations  
 218 with MISR simulator output, ta and zg indicate those where the atmospheric temperature and  
 219 geopotential fields are used respectively

220 The model AMIP output used here are available for download through the ESGF CMIP6  
 221 database (<https://esgf-node.llnl.gov/projects/cmip6/>) and MISR observation data are available  
 222 from the NASA Langley archive (<http://asdc.larc.nasa.gov/project/MISR/>). The SSP 585  
 223 simulation with the MISR-COSP simulator was performed as an independent run by each  
 224 modeling center, and is available at: [https://atmos.uw.edu/~roj/MISR\\_observations/](https://atmos.uw.edu/~roj/MISR_observations/).

225

## 226 2.1 The Weighted Cloud Top Height (WCTH) Metric

227

228 MISR and the MISR simulator parse cloud occurrence into a fixed set of CTH and (total  
 229 column) optical depth bins. To assess a trend in CTH, we calculate a cloud-fraction weighted  
 230 average CTH (WCTH) from the histogram data as given below in Equation 1. Here we define  
 231 high clouds as those above 9 km in the tropics (between -20° and 20° latitude), above 7 km in the  
 232 subtropics (±20° to ±40° latitude), and above 5 km for all latitudes poleward of ±40° in both  
 233 hemispheres. The MISR histogram is first integrated over (some desired range of) optical depth  
 234 to obtain the cloud occurrence ( $CF_z$ ) associated with each MISR height bin (with height  $CTH_z$ ).

235

$$236 \quad WCTH = \frac{\sum_{z>thresh}(CTH_z \times CF_z)}{\sum_{z>thresh}(CF_z)} \quad (1)$$

237

238 The WCTH describes the average height of high clouds, when a high cloud occurs, and is  
 239 independent of the total amount of high cloud. The altitude thresholds chosen above align with  
 240 bin boundaries used in the MISR histogram and capture the peak in high-cloud occurrence  
 241 (Aerenson, 2021; Marchand et al., 2010), and are high enough to avoid issues related to mid-  
 242 level clouds. Specifically, the rate of change of the CTH of mid-level clouds may not be the  
 243 same as high clouds, and at a practical level, clouds crossing the threshold – whether it is low-  
 244 level clouds shifting into mid-levels or mid-level clouds into high-levels can create artifacts in  
 245 the WCTH metric. Except where otherwise stated, the WCTH is calculated using all clouds that  
 246 would be routinely observed by MISR (meaning all marine clouds with optical depth greater than  
 247 0.3). In the analysis WCTH is calculated over various bands of latitude, and different regions are  
 248 examined in an effort to determine where MISR will first be able to observe a climate trend as  
 249 temperature may increase at different rates in different regions, which may lead to different times  
 250 of emergence.

251

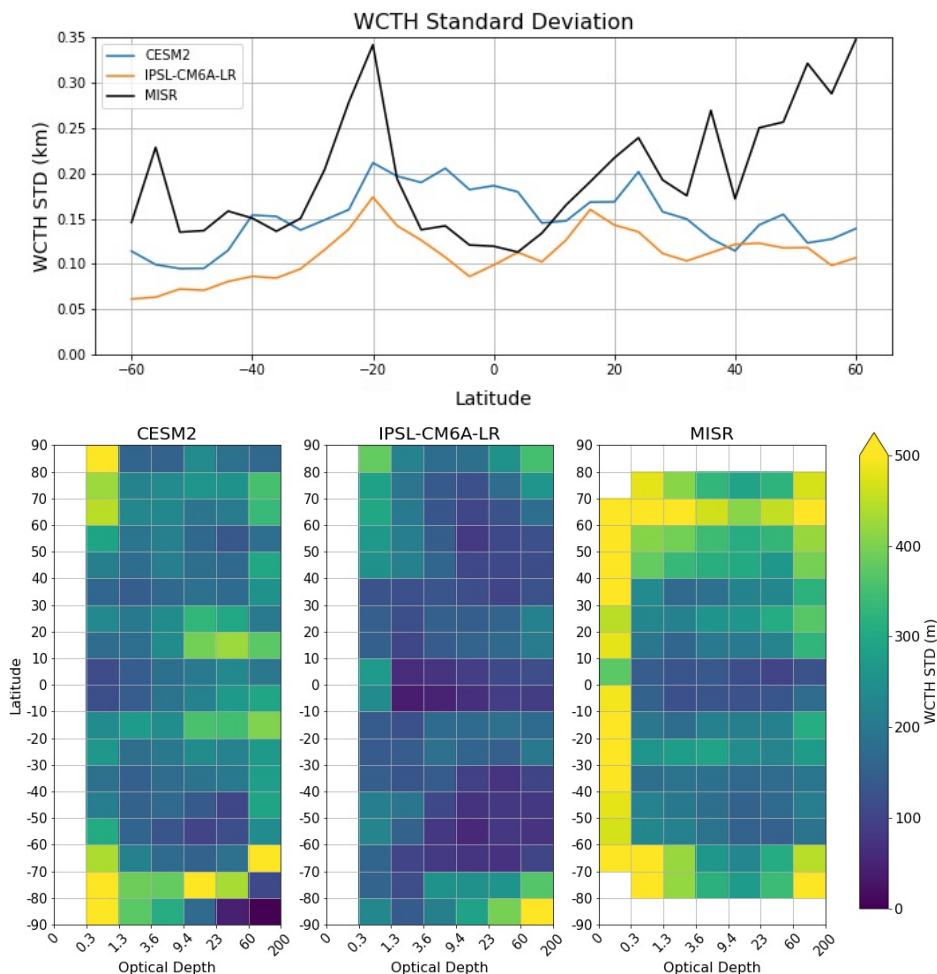
## 252 2.2 Variability of WCTH in Models and Observations

253 Determining the time of emergence (TOE) means finding the time at which a true change (in  
 254 the present case an increase in CTH) can be differentiated with confidence from apparent  
 255 changes that might arise from random fluctuations due to internal variability, measurement error,  
 256 or sampling. Thus, to estimate TOE for the MISR observations based on model simulations, we

257 want the model simulations to realistically represent both the climate trend change (the signal)  
258 and the variability (the noise).

259 The top row of **Figure 1** shows the zonal mean standard deviation of WCTH for both models  
260 and the MISR observations. Here the results have been calculated using a 4° grid and are based  
261 on monthly data over the period April 2000 to 2015, which are the years that overlap the portion  
262 of the model simulation forced with historical emissions and the observational record. The data  
263 is deseasonalized by subtracting the mean seasonal cycle before the standard deviation is  
264 calculated. Overall, the observations have larger variability in WCTH over most of the  
265 subtropics and midlatitudes than both models. However, in the tropics (between -20° and 20°)  
266 CESM2 appears to have greater variability than the observations, while IPSL has slightly less  
267 variability.

268 We note that the MISR simulator acts as if it sees the entire globe at once, while in reality  
269 MISR can only see a narrow swath below the satellite at any given time. However, assuming  
270 there is no correlation between the MISR sampling and WCTH (which seems a safe assumption)  
271 and gaussian statistics, the standard deviation in WCTH measured by MISR will be given by  
272  $\sigma_{internal}/\sqrt{2 * n_{eff} - 2}$ , where  $\sigma_{internal}$  is the standard deviation of the internal variability in  
273 WCTH and  $n_{eff}$  is the effective number of independent samples collected by MISR. While  
274 strictly speaking the above formula for sampling variability only applies to gaussian distributed  
275 variables, in the general form the variability can be expected to decrease asymptotically as a  
276  $1/\sqrt{n_{eff}}$  (e.g. Cho et al., 2005). MISR completes roughly 15 orbits each day, sampling a  
277 different set of longitudes in each orbit. Even if each day constitutes only three to four  
278 independent samples, over the course of the month that suggests the increase in variability  
279 resulting from the MISR sampling would be 10% or less of the total variability. The differences  
280 in the top panel of **Figure 1** are clearly much greater than 10%, and we conclude that the  
281 differences in WCTH standard deviation seen in **Figure 1** are likely a result of differences in  
282 internal variability (between models and between the models and reality) and not a sampling  
283 effect.



284  
 285 **Figure 1** Top row: Standard deviation of zonal mean WCTH over all optical depth on a 4-degree  
 286 grid. Bottom row: Standard deviation of zonal mean WCTH on a 10-degree grid separated by  
 287 optical depth

288 In later analysis the data is separated into the different MISR optical depth ranges. The  
 289 standard deviation of WCTH separated by latitude and optical depth is shown in the bottom row  
 290 of **Figure 1** for the models and observations (again calculated for the historical period). The  
 291 latitudinal variability seen in the top panel in **Figure 1** is also clear in the bottom plots as well,  
 292 but with the additional detail of seeing how variability changes with optical depth. In the MISR  
 293 observations the high variability in the northern hemisphere poleward of 40° occurs at all optical  
 294 depths, however there is relatively lower variability between 9.4 and 23, which is the most  
 295 heavily occupied optical depth category in this region. The magnitude of the variance is much  
 296 lower in the SH poleward of 40° (compared to NH), but with the optical depth dependence  
 297 (lowest variability between 9.4 and 23) being the same.

298 In the tropics (-10° to 10°) there are fairly small differences in the MISR observed  
 299 variability at different optical depths (except for the most tenuous cloud with optical depths  
 300 below 0.3, which are not used in the analysis because they are not reliably detected). Both  
 301 models show greater dependence on optical depth in the tropics. CESM has larger variability  
 302 (than observations) at optical depths greater than 3.6 and IPSL has lower variability (than  
 303 observations) for optical depths between 1.3 and 23. In the subtropics (20° to 40° in both

304 hemispheres) there is generally greater variability than in the tropics at virtually all optical depths  
305 for the MISR observations as well as the models. CESM shows a much higher variability for  
306 cloud with optical depth greater than 9.4, which is not seen in the observations or IPSL.  
307 Generally, IPSL shows less variability than the observations for optical depths greater than 1.3 at  
308 all latitudes. As noted in the top row of **Figure 1** the models produce much less variability in the  
309 northern hemisphere midlatitudes and the southern hemisphere subtropics than is seen in  
310 observations.

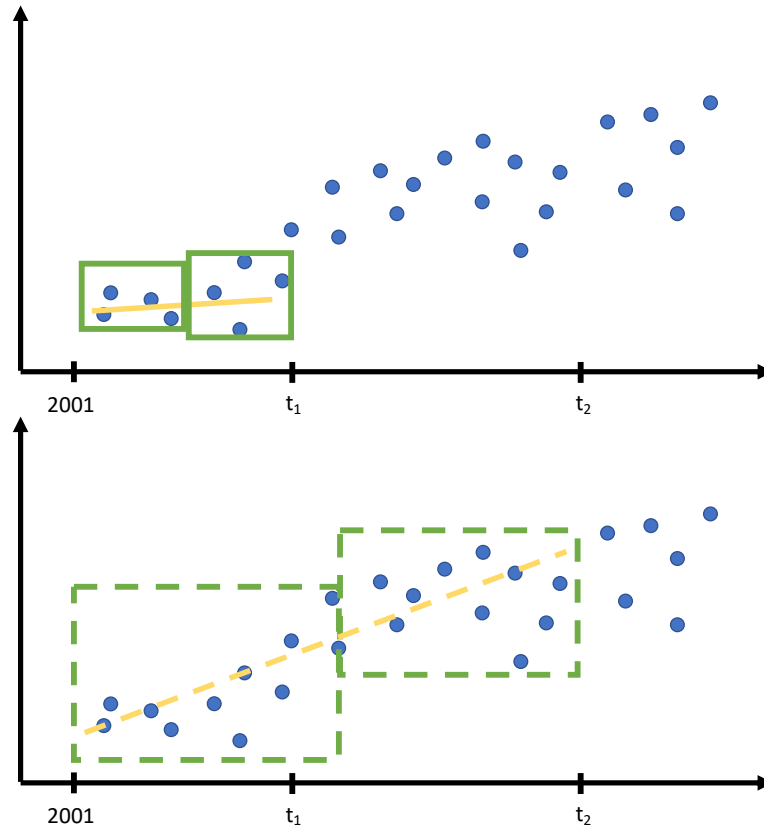
311

### 312 2.3 Calculating Time of Emergence (TOE)

313 The WCTH metric is used to determine when MISR would be able to detect a change in  
314 CTH with a high degree of confidence, if high cloud CTH increases as predicted by the climate  
315 models. Timeseries of WCTH are constructed for various latitude bands by first summing  
316 histogram counts over the region in question in each month. WCTH is then calculated from each  
317 monthly histogram using the approach described in Section 2.1. The MISR histograms give  
318 cloud occurrence such that the sum of the component values gives the total cloud fraction, and  
319 therefore summing the histograms over the target region yields a WCTH that is weighted by the  
320 high cloud occurrence in the model grid cells (latitude, longitude bins).

321 The seasonal cycle is removed from the WCTH timeseries by subtracting the mean value at  
322 each month of the year (averaged over every year along the timeseries) from the initial WCTH  
323 timeseries. Then the total mean over all months is added back to restore the timeseries to the  
324 correct mean state. After which, the time of emergence (TOE) is obtained as the point in time  
325 when a pair of statistics, the slope and  $\Delta_{\text{mean}}$  (described below and shown in **Figure 2**), are both  
326 nonzero to 95% confidence and remain nonzero for the remaining duration of the timeseries.

327 The slope statistic is defined as the slope of a least-squares linear regression line. The  $\Delta_{\text{mean}}$   
328 statistic is defined as the difference between the mean value calculated over the second half of  
329 the time series minus that averaged over the first half of the timeseries. Each statistic is  
330 calculated at each year along the WCTH timeseries for all previous data. So, for every year, both  
331 statistics are calculated from the timeseries starting in April of 2000 (the start of MISR  
332 retrievals) and ending on the year in question. The process of calculating the statistics along each  
333 year of the timeseries is illustrated in **Figure 2**.



334  
335  
336  
337  
338  
339

**Figure 2** A diagram of how the two statistics are calculated for each year of the simulation. The top panel shows how the statistics are calculated for some year  $t_1$  then the bottom panel shows the same for some later time  $t_2$ . In both, the  $\Delta\text{mean}$  statistic is the difference between the mean values encompassed by the green rectangles, and the slope statistic is the slope of the yellow line.

340  
341  
342  
343  
344  
345  
346  
347  
348  
349  
350  
351  
352  
353  
354  
355  
356

At each year 95% confidence intervals are calculated for each statistic using a moving-blocks bootstrap technique, which is a resampling scheme that is designed to be used with autocorrelated data. By resampling over a specific sized block of data, the effect of any autocorrelation on time scales shorter than the block length is included in the confidence interval calculation. A detailed description of the method is given by Wilks (1997). An examination of the autocorrelation of the WCTH timeseries is given in the supplementary materials. Based on this examination, a block length of 24 months was selected as it captures well over 75% of the correlation. The resampling is performed 5000 times, and then the 1-tailed 95% confidence limit is calculated from the resampled distribution.

This analysis is conservative in that for TOE to be designated, both the  $\Delta\text{mean}$  and slope statistics are required to remain nonzero to 95% confidence for the remainder of the model simulation. Of course, in application one doesn't know the future so the "remainder" isn't known. However, we find it to be rare for both of our metrics to be triggered with significance and even one test statistic to lose significance later in the simulation. When that did occur, the loss-of-significance was delayed less than 2 years.

## 2.4 Scaling of Model CTH Variability to Match Observations

357 It was found in Section 2.2 that in many regions there is greater variability in the  
 358 observational record than is produced in the models running the MISR simulator. It is essential to  
 359 represent the variability that MISR observes accurately to calculate a realistic time of emergence  
 360 for a trend in WCTH. Consequently, we increase the variance in the simulated time series as  
 361 follows, in which the time series of WCTH is treated as the sum of a forced and random term:  
 362

$$WCTH^{MISR}(t, \varphi) = WCTH_{forced}^{true}(t, \varphi) + \partial WCTH^{MISR}(t, \varphi) \quad (2a)$$

363 and

$$WCTH^{model}(t, \varphi) = WCTH_{forced}^{model}(t, \varphi) + \partial WCTH_{var}^{model}(t, \varphi) \quad (2b)$$

364 where  $\partial WCTH$  is a random variable, and  $WCTH_{forced}$  is the forced response at some time and  
 365 taken over some set of model grid-cells denoted by  $\varphi$ . Ideally  $\partial WCTH^{MISR}(t, \varphi)$  would be well  
 366 represented by  $\partial WCTH^{model}(t, \varphi)$ , however this was not found to be the case in Section 2.2  
 367 where the variability in the models was found not to match well with the observations during the  
 368 historical period (2001-2015). Thus, a linear approach is taken to matching the observed and  
 369 simulated variabilities.  
 370

$$WCTH^{model}(t, \varphi) = WCTH_{forced}^{model}(t, \varphi) + R(\varphi) * \partial WCTH_{var}^{model}(t, \varphi) \quad (3a)$$

where

$$std[\partial WCTH^{MISR}(t, \varphi)] = R(\varphi) * std[\partial WCTH_{var}^{model}(t, \varphi)] \quad (3b)$$

371  $std[-]$  denotes taking the standard deviation of the timeseries,  $R(\varphi)$  is a constant (in time) that  
 372 we refer to as the *scaling factor*. We determine the scaling factor by finding the ratio of the  
 373 observed and modelled variability during the historical period. More specifically, the scaling  
 374 factor is calculated by first removing any linear trend from the WCTH time series for both the  
 375 observations and the model simulations. After this trend removal, the standard deviation is  
 376 calculated from each times series, and  $R(\varphi)$  is calculated as the ratio of the observed standard  
 377 deviation to the modeled standard deviation using only the historical period. To produce a  
 378 conservative estimate for TOE, the regions where the variability is greater in the models than the  
 379 observations are left unchanged. That is, we calculate  $R(\varphi)$  as:  
 380

$$R(\varphi) = std[\partial WCTH^{MISR}(t_{obs}, \varphi)] / std[\partial WCTH_{var}^{model}(t_{obs}, \varphi)] \quad (4a)$$

$$if R(\varphi) < 1, then R(\varphi) = 1 \quad (4b)$$

381 Where  $t_{obs}$  spans from April 2000 to 2015.

382 It is important to note that this method does allow for the variability to change in time. The  
 383 standard deviation is not forced to match the observed standard deviation for the entire run;  
 384 rather the standard deviation of the entire run is scaled up by a constant factor so that the  
 385 standard deviation matches observations during the historical period, and the variability after  
 386 2015 can be different from the historical period. After this technique is applied to the data, the  
 387 time of emergence analysis, as described in Section 2.3, is performed on the WCTH time series  
 388 to determine TOE.

389 On a minor note, we also examined an additive model for increasing the variability:  
 390

$$std[\partial WCTH^{MISR}(t, \varphi)] = std[\partial WCTH_{var}^{model}(t, \varphi)] + C(\varphi) \quad (5)$$

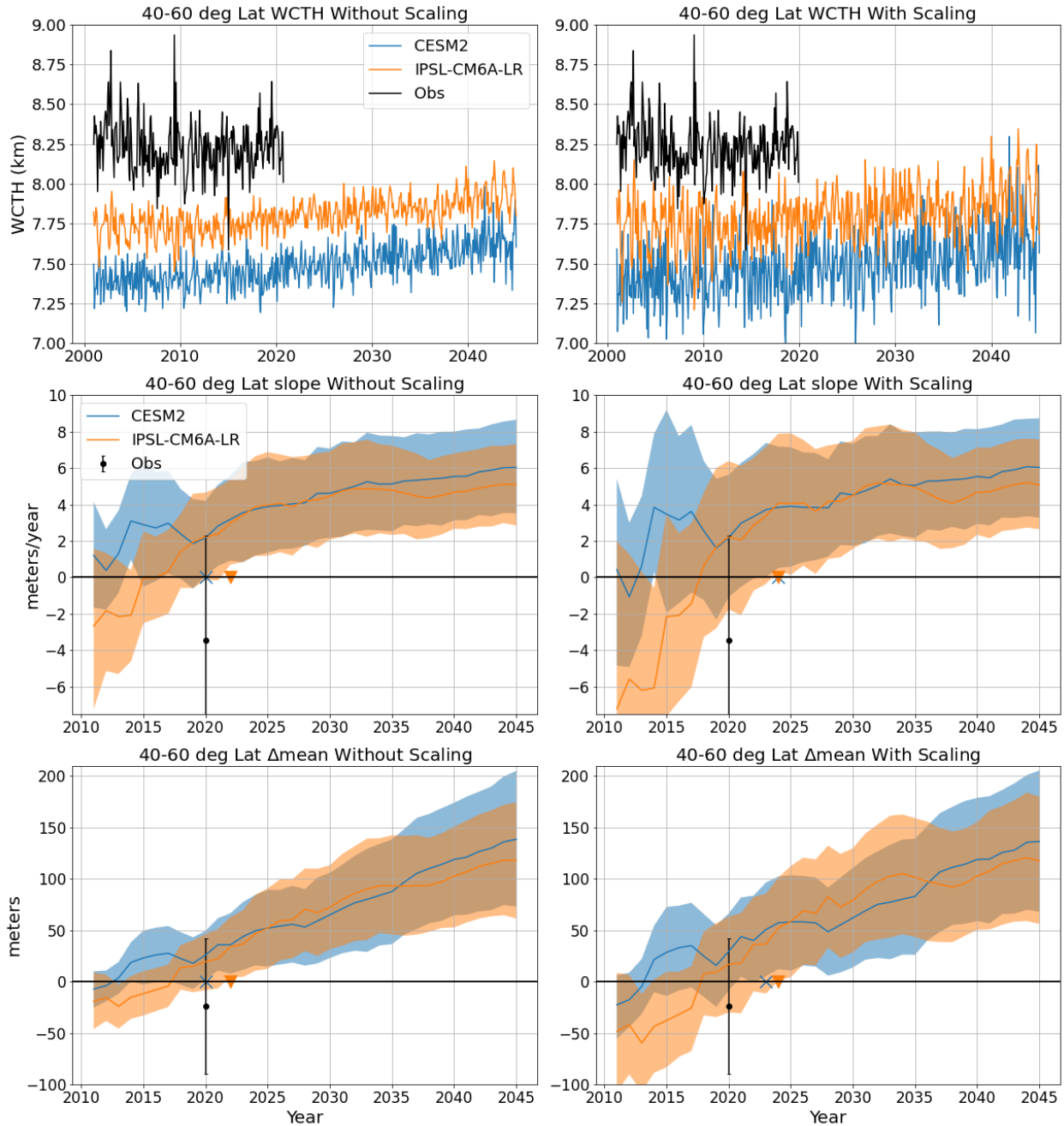
391 Where  $C(\varphi)$  is a constant *additive factor*. The scaling and additive methods result in nearly  
 392 identical TOE, and so only the multiplicative scaling is presented here. But a detailed  
 393 description of the additive approach is available in the thesis that accompanies this work  
 394 (Aerenson, 2021).

395

### 396 **3. Time of Emergence (TOE) Results for CESM2 and IPSL-CM6A-LR**

397

398 The methods described in Section 2 were applied to outputs from CESM2 and IPSL SSP 585  
 399 simulations to predict when MISR should be capable of detecting a trend in cloud-top-height.  
 400 The trend analysis is carried out over various regions and latitude bands, both with and without  
 401 the variance adjustment described in Section 2.4. In **Figure 3** the timeseries of WCTH is shown  
 402 for the Northern midlatitudes, as well as the timeseries of the  $\Delta$ mean and slope statistics, with  
 403 their 95% confidence intervals. The left and right columns show the results without and with the  
 404 variance scaling respectively. The top panels show the observed and model WCTH time series.  
 405 Comparing the model WCTH time series between the top left and right panels (comparing the  
 406 orange and blue lines) shows how variance scaling has substantially increased the variability in  
 407 the model WCTH time series. As is also obvious, the observed WCTH (black line) is greater  
 408 than the WCTH calculated from the models, with the observed WCTH being above 8 km while  
 409 the model WCTH are generally below 8 km. The models have a variety of biases with respect to  
 410 the observations, including the WCTH. We provide a brief examination of model biases in the  
 411 supplementary material (Text S1, Figures S1 and S2), and will discuss the topic further in the  
 412 concluding section.



413  
414  
415  
416  
417  
418  
419

**Figure 3** Upper left: WCTH timeseries for the MISR observational record and both models, averaged over the NH midlatitudes. Upper right: Same as upper left, but with the variance scaling applied. Middle left: slope statistic and confidence intervals calculated at each year starting in 2010 for each model, shown in black is the statistic calculated for the full observational record. Middle right: same as middle left, but with the variance scaling applied. Bottom row: The  $\Delta$ mean statistics are shown with and without the variance scaling applied

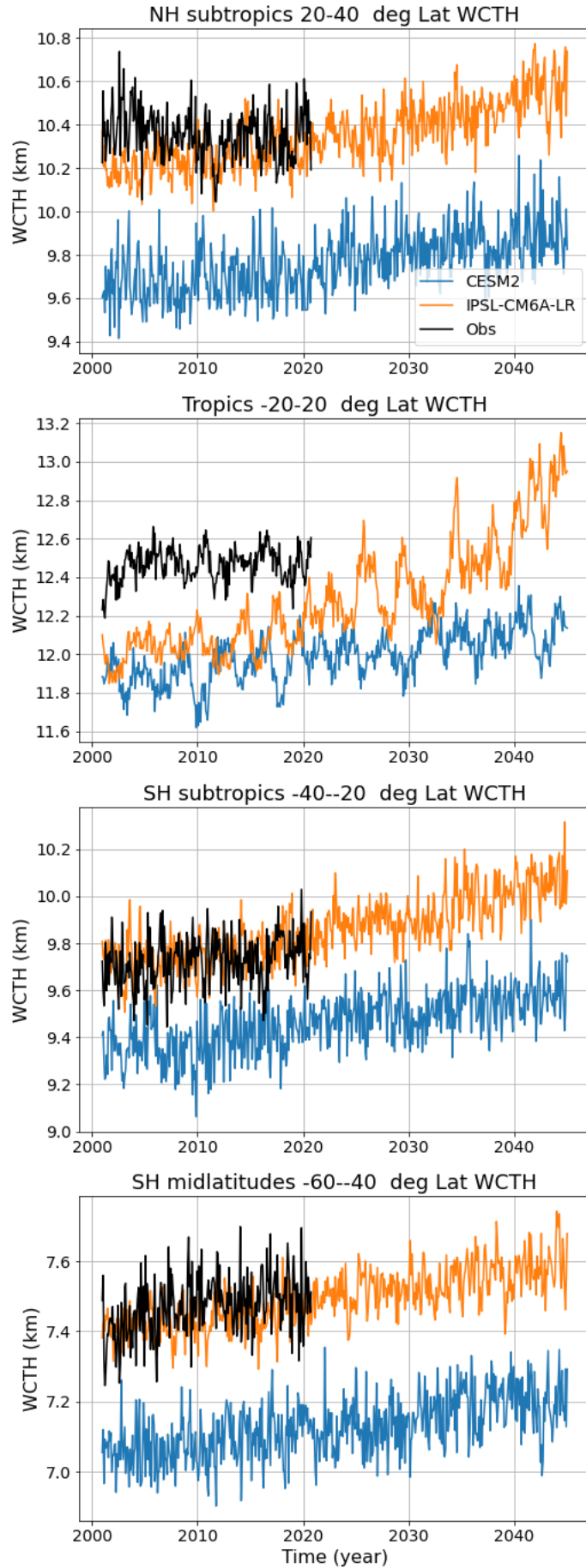
420  
421  
422  
423

The lower two rows of plots show the two statistics used to determine TOE. Here the colored lines are the slope (middle panels) and  $\Delta$ mean statistic (bottom panels) calculated for the time series made from the time of the earliest of MISR observation (April 2000) and ending in each year from 2010 to 2045. The shading indicates the 95% confidence limits, which were

424 found using the moving block bootstrap technique, described in Section 2.3. As one expects, the  
425 shaded region in the right panels is wider, because of the scaled-up variability. The TOE is  
426 defined as the time when the confidence intervals of both statistics exceed zero, and remain  
427 above zero until the end of the simulation. The TOE date for each statistic is marked by an X or a  
428 triangle for CESM2 and IPSL respectively. The black dot and bars show the slope and  $\Delta$ mean  
429 statistic (and 95% confidence interval) for the current MISR observational record, ending in June  
430 of 2020.

431 The overall TOE is determined by finding the point at which both statistics are significant.  
432 When the variance scaling is not applied to the analysis, TOE occurs at 2020 in CESM2, and at  
433 2022 in IPSL, and the TOE is delayed by the variance scaling, so that when the variability is forced  
434 to match the observations, both models predict TOE at 2024.

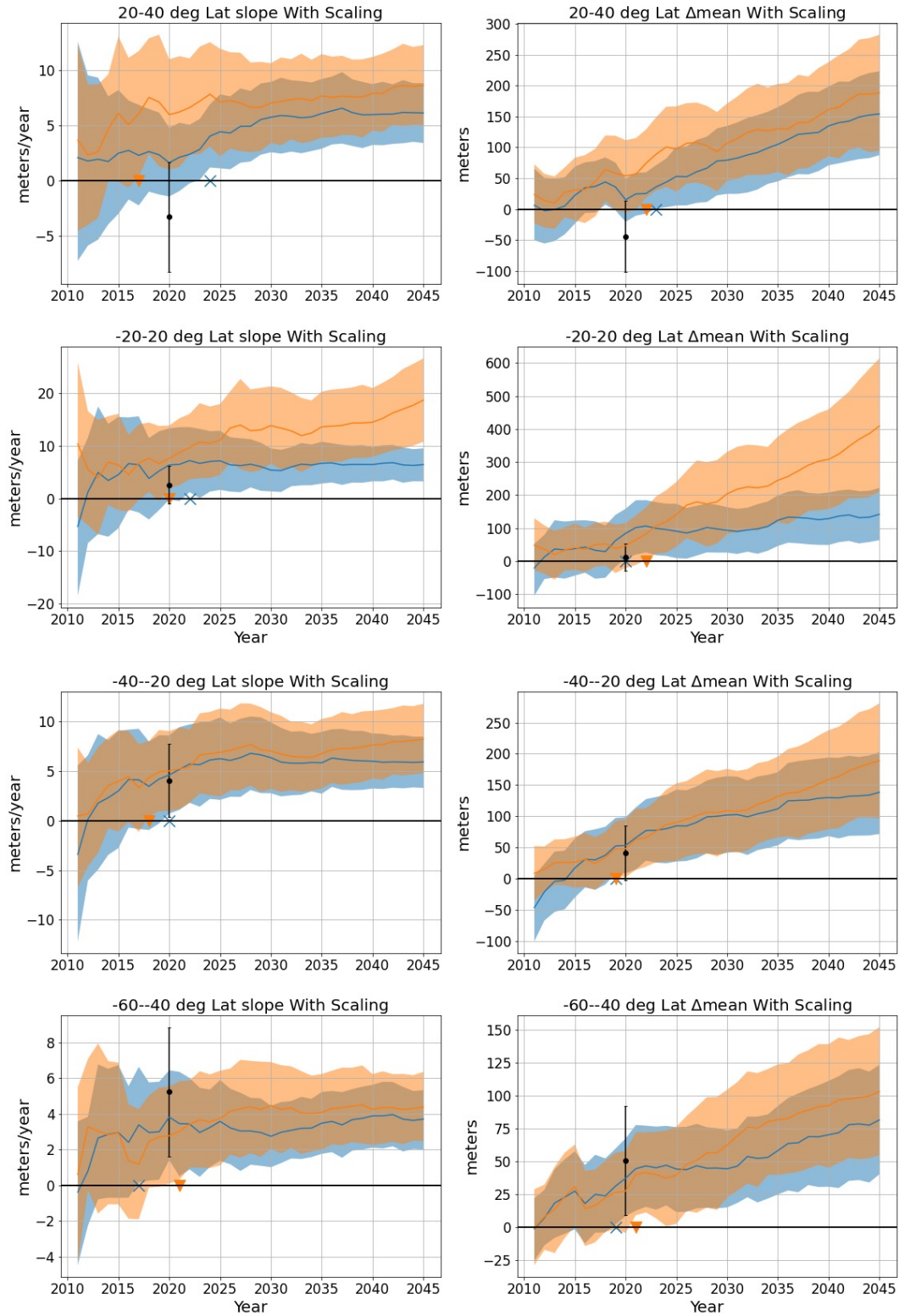
435 The timeseries of WCTH for four additional latitude bands are shown in **Figure 4**, with  
436 slope and  $\Delta$ mean statistic in **Figure 5**. Here only results with variance scaling are shown.  
437



439 **Figure 4** *Timeseries of WCTH averaged over subtropics and midlatitudes. The observations are*  
440 *shown alongside the model output*

441 In the tropics (second panel of **Figure 4**) both models display variations in WCTH that  
442 are correlated on longer scales than at other latitudes. This is due to ENSO. Both models initially  
443 begin with a similar upward trend in WCTH, but after 2035 the WCTH in IPSL increases more  
444 rapidly than CESM2 in the tropics. We discuss this large change further in Section 4, but as we  
445 will see momentarily it is not important for the estimated TOE, as the increase in CTH becomes  
446 detectable in both models before 2025. Overall, the two models behave much more similarly to  
447 each other in the subtropics and midlatitudes than in the tropics.

448 **Figure 5** shows how the slope and  $\Delta$ mean statistics change during the simulation and  
449 their accompanying 95% confidence intervals. As with **Figure 4**, the results shown in **Figure 5**  
450 do have the variance scaling applied. The results of the TOE calculation, with and without  
451 variance scaling, are given in **Table 2**. Overall, **Figure 5** shows a similar pattern of CTH  
452 increase in each model simulation, despite the climatological (base state) differences between the  
453 models. The rate of CTH increase is typically slightly greater for IPSL than it is for CESM2, but  
454 the difference is small, and is well within the 95% confidence intervals for all regions. Both  
455 models predict that MISR should be capable of observing a trend in CTH in all latitude bands by  
456 2024. For the most part the models are in agreement within a 2-year range. The variance scaling  
457 does matter, and delays the detection as much as 4 years, depending on the model and the  
458 latitude band, and is most significant in the Northern Hemisphere, where variability of observed  
459 WCTH is larger than that simulated by the models.



460  
461  
462  
463

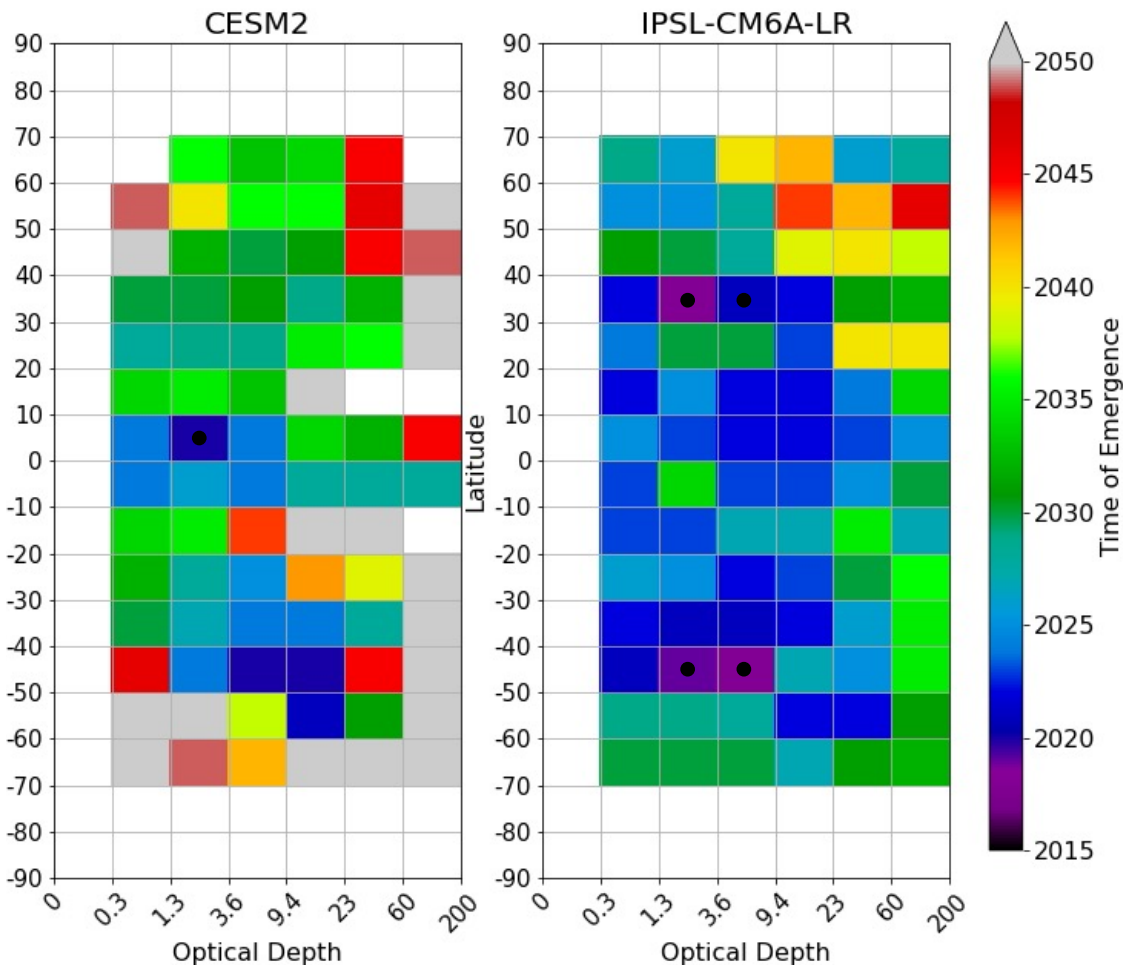
**Figure 5** Plots of the same format as the bottom two rows of **Figure 2** but shown over the other remaining regions. Right column is the slope statistic at each latitude range, left column is the  $\Delta$ mean statistic. The plots shown do include the variance scaling

464 With variance scaling, TOE is earlier in the SH than the NH, and the model results  
 465 suggest that MISR results (which currently extend through June of 2020) should have detected,  
 466 or be close to detecting a change in the SH. Indeed, the observations results in **Figure 5** (the  
 467 black dot and bar) show that MISR has observed an increase in CTH that slightly or nearly  
 468 exceed the 95% confidence for a non-zero change in the SH, suggesting that there has been a  
 469 statistically significant increase in CTH. However, analysis by Geiss & Marchand (2019) suggest  
 470 that MISR changes in SH may be an El Niño Southern Oscillation (ENSO) signal rather than a  
 471 broad increase in CTH. This will be further discussed in the concluding section.  
 472

Variance Method	CESM2		IPSL-CM6A-LR	
	Model's Innate Variance	With Variance Scaling	Model's Innate Variance	With Variance Scaling
NH midlatitudes	2020	2024	2022	2024
NH subtropics	2022	2024	2018	2022
Tropics	2022	2022	2022	2022
SH subtropics	2020	2020	2018	2019
SH midlatitudes	2019	2019	2018	2021

473 *Table 2 TOE as calculated from each model at 5 different latitude bands. TOE calculations were*  
 474 *performed with and without the variance scaling described in Section 2.4*

475 To this point all analysis has been performed on the full optical depth range that is  
 476 confidently detected by MISR (greater than 0.3). We would like to understand if there are  
 477 preferential optical depths and narrower latitudes where early trend emergence may occur. In  
 478 **Figure 6**, the same TOE analysis is performed on WCTH calculated on smaller latitude ranges  
 479 and at specific optical depths to understand the zonal and optical depth structure of the TOE.  
 480 Variance scaling is applied, with scale factors calculated for each latitude and optical depth  
 481 range. Narrowing the analysis to smaller latitude and optical depth ranges largely produces later  
 482 TOE than the broad ranges shown in **Table 2**. The few latitudes and optical depth ranges where  
 483 TOE is earlier than those given in **Table 2** are marked with a black dot. There is only 1 such  
 484 range for CESM2, and only 4 for IPSL. With 84 latitude and optical depth bins occupied, and a  
 485 95% confidence threshold, one expects by random chance that a few bins would result in an  
 486 early TOE (and these few earlier detections would not pass a field significance test). In general,  
 487 the CESM2 and IPSL models produce very different structure of TOE in latitude and optical  
 488 depth and there is no clear pattern in optical depth that results in earlier detection. While not  
 489 presented here, in the accompanying thesis work (Aerenson, 2021) we did examine other  
 490 approaches to improve TOE by preferentially selecting longitudinal regions or optical depth  
 491 ranges with relatively low observational variance and found this had little or no benefit relative  
 492 to using full (over ocean) averages of fairly wide (at least 20°) latitudinal bands. And while  
 493 MISR observations have not been processed over land (owing to difficulties in the retrieval  
 494 optical depth over land), we found no advantage to focusing on CTH over land in the model data.  
 495 Based on these limited data, we conclude that the most effective way to detect trends in CTH is  
 496 through broadly averaged zonal means that can be routinely seen by MISR.  
 497



498  
 499 **Figure 6** Time of Emergence calculation is performed on zonal mean WCTH calculated on a 10-  
 500 degree grid, for each individual optical depth bin with the variance scaling applied. Results of  
 501 such calculations are shown as the pixel coloring, white pixels show regions where there is  
 502 insufficient cloud to perform the TOE calculation which is defined as more than one tenth of the  
 503 months having no cloud in that given category. Black dots indicate pixels corresponding to TOE  
 504 earlier than the broad zonal mean value given in **Table 2**

505  
 506 **4. Consistency of Rising WCTH with the FAT Hypothesis**  
 507

508 As described in the background material, the FAT hypothesis asserts that the CTH of high  
 509 clouds will remain at a nearly fixed temperature. This section asks whether the change in CTH  
 510 seen in the models is consistent with this hypothesis.

511 To do this, the WCTH calculated from the model output is compared with two forms of  
 512 synthetic WCTH that are calculated assuming a perfect FAT response in CTH, as well as in a  
 513 perfect Fixed-Anvil-Pressure (FAP) response. The synthetic WCTH that follows a perfect FAT  
 514 response is calculated by first averaging the temperature profile in the cloudy part of each region.  
 515 This is done by calculating the cloud-fraction-weighted average of the temperature profile over  
 516 the region of interest:

$$T(z_{model}, t) = \frac{\sum_{lat, lon}(ta(z_{model}, lat, lon, t) \times \sum_{z>thresh} CF_z(lat, lon))}{\sum_{z>thresh, lat, lon}(CF_z(lat, lon))} \quad (6)$$

517  
518  
519 where  $ta$  is the model's temperature profile on its native height grid, where  $z_{model}$  represents a  
520 level on that model's height grid,  $CF_z$  is the MISR high cloud fraction at each grid level (found  
521 by summing MISR CTH-OD histogram components at all optical depths), averaged over the  
522 observational period 2001-2015, the subscript  $[-]_z$  represents the discrete heights of the MISR  
523 CTH-OD histogram, and  $T(z_{model}, t)$  is the resulting average temperature profile of the cloudy-  
524 sky portion of the region of interest. This profile is then interpolated to match the vertical  
525 spacing of the MISR CTH retrievals, so  $T(z_{model}, t)$  is averaged over the observational period  
526 and linearly interpolated on to the MISR vertical grid denoted below as  $T_z$ , and this is used to  
527 calculate the weighted cloud-top-temperature (WCTT) for the MISR profiles in a similar way to  
528 the WCTH for the observational period as:

$$WCTT = \frac{\sum_{z>thresh}(T_z \times CF_z)}{\sum_{z>thresh}(CF_z)} \quad (7)$$

531  
532 Finally, the FAT WCTH is calculated by assuming WCTT remains constant over time.

533 Specifically, the FAT WCTH is taken as the altitude where  $T(z_{model}, t)$  matches WCTT from  
534 the historical period, found via linear interpolation between the levels of  $T(z_{model}, t)$ .

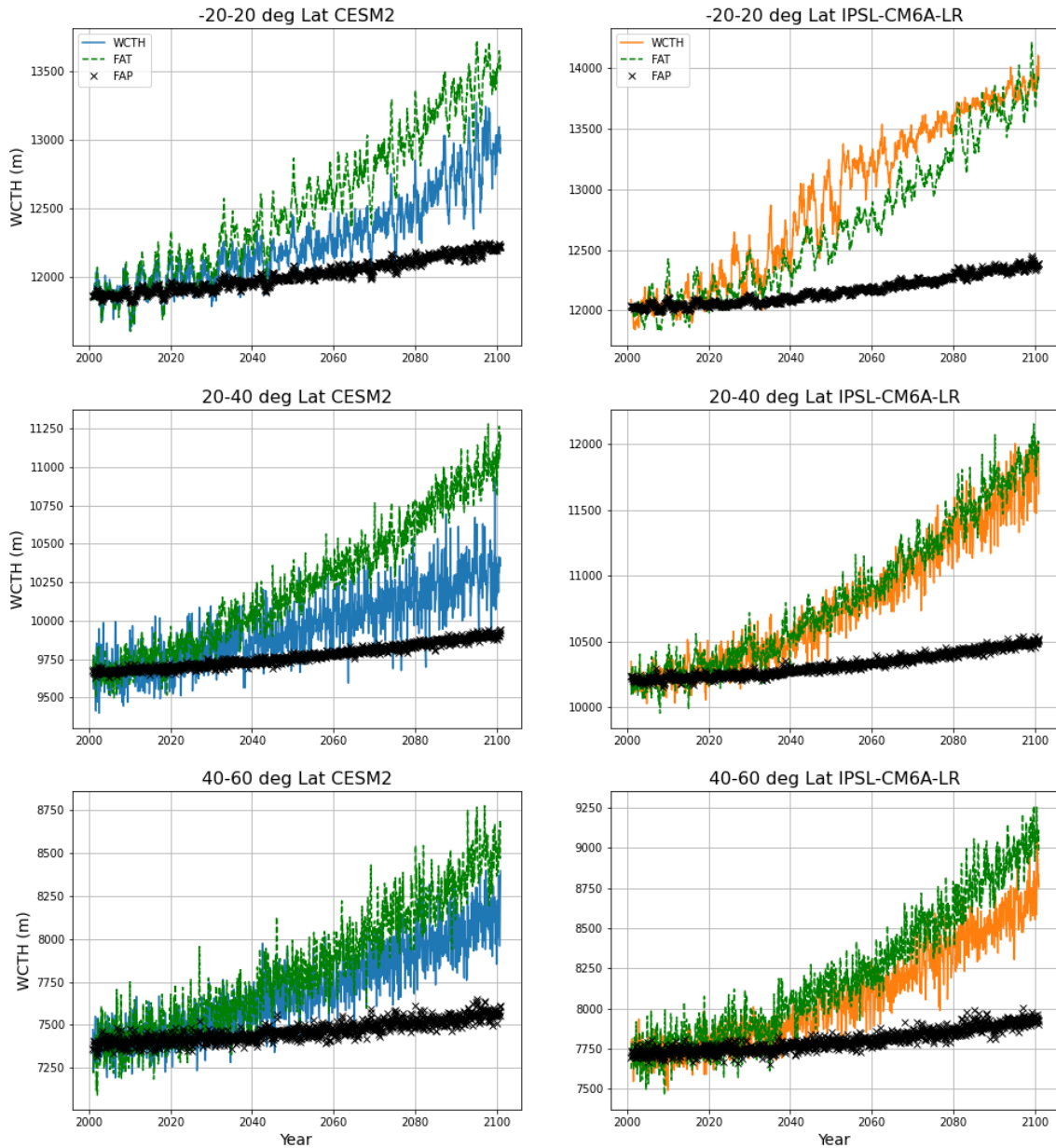
535 The FAP WCTH is calculated using the same method as the FAT WCTH, except the  
536 pressure profile rather than the temperature profile is used, so that FAP WCTH is equivalent to  
537 assuming clouds remain at a constant pressure with warming.

538 The results of the FAT and FAP calculation are shown in **Figure 7** along with the WCTH  
539 calculated directly from the MISR simulator output for the CESM2 and IPSL models which ran  
540 the SSP 585 scenario with the MISR simulator. The results are shown for the tropics (top panels)  
541 and Northern Hemisphere subtropics (middle panels) and midlatitudes (bottom two panels).

542 Results for the Southern Hemisphere are not shown, but are characteristically similar. A  
543 confirmation of the FAT hypothesis would appear as the directly simulated WCTH (blue/orange  
544 lines) increasing at the same rate as the WCTH calculated with a fixed temperature profile (green  
545 line, labeled FAT). In the subtropics and midlatitudes, the WCTH of both CESM2 and IPSL  
546 WCTH increases slightly slower than FAT, but faster than the FAP WCTH, and is consistent  
547 with the behavior expected for PHAT.

548 The situation is more complicated in the tropics of the IPSL model. In IPSL, the WCTH  
549 increases at a rate faster than is suggested by FAT. More specifically, the increase in WCTH is  
550 much faster between 2030 and 2050, but then slows down at 2050 such that by the end of the  
551 century WCTH has increased by the same amount as the FAT projection. This response is  
552 examined in detail in the supplementary materials (**Text S3 and Figure S5**) as well as the  
553 accompanying thesis (Aerenson, 2021), and is an artifact of the MISR discretization that arises  
554 when the vertical distribution of high clouds occurrence is narrow compared with the size of the  
555 discrete MISR CTH categories (which is 2 km in the upper troposphere). The artifact does not  
556 appear in the CESM2 results because the vertical distribution of high clouds is wider than in  
557 IPSL, and compares better with the observed distribution.

558



559  
560  
561  
562  
563  
564

*Figure 7* WCTH is shown for each model alongside the synthetic WCTH that is calculated assuming a perfectly FAT condition and FAP condition. Timeseries are shown for the tropics and both Northern Hemisphere regions, and are extended to include the entire 21<sup>st</sup> century. The seasonal cycle is removed via 25-year averages so that change in the seasonal cycle does not impact the timeseries shown

565  
566  
567  
568  
569  
570  
571

In spite of the discretization problems, the increase in CTH based on the assumption that the FAT hypothesis appears to be a reasonably good approximation, at least for the period up to 2040, though we expect the FAT assumption will result in a somewhat earlier than true TOE. We exploit this in the next section to extrapolate or create synthetic WCTH timeseries for several additional models that ran the MISR simulator during AMIP simulations, but did not run the MISR simulator during their SSP 585 simulations in order to gauge the spread in TOE one might expect from a larger set of models.

## 5. Synthesized WCTH Forecast Using AMIP runs and the FAT Hypothesis

As discussed in Section 2.2, the detection of change in CTH can be viewed as a signal to noise problem. In the analysis presented in Section 3, the signal was based on output from two models, CESM2 and IPSL-CM6A-LR, which ran the MISR simulator as part of their SSP 585 simulations. However, both IPSL-CM6A-LR and CESM2 warm quickly relative to other climate models and have above-average Equilibrium Climate Sensitivity (ECS): CESM2 has an ECS of 5.2 K per doubling CO<sub>2</sub> and IPSL-CM6A-LR has an ECS of 4.6 K per doubling CO<sub>2</sub> (Meehl et al., 2020). One presumes the TOE would occur later if warming occurs more slowly, and in general there is likely to be some variability (spread) in the rate of CTH increase between models per degree of increase in surface temperature. To investigate these possibilities, we synthesize WCTH timeseries for models that (1) produced MISR simulator output for the AMIP run and (2) ran the SSP 585 simulation (regardless of whether or not the MISR simulator output was produced) under the assumption that high cloud CTH will rise with a fixed temperature distribution. As shown in Section 4 the change in MISR simulated WCTH in the CESM2 and IPSL-CM6A-LR is reasonably well approximated by a FAT-like increase in CTH (at least out to 2040). In addition to CESM2 and IPSL-CM6A-LR, the models examined in this section are the MRI-ESM2-0, CanESM5, CNRM-CM6-1, CNRM-ESM2-1, and BCC-CSM2-MR. The synthetic WCTH time series are created following the approach described in Section 4, except instead of calculating the WCTT based on the historical period (as was described in Section 4), the WCTT is calculated using the AMIP run from 2001 to 2015. Then the temperature profile from the historical and SSP 585 fully coupled model simulations are used to calculate the height at which the AMIP WCTT occurs in the historical and SSP 585 simulations from 2001 to 2100; and the same TOE analysis used in Section 3 is applied to the AMIP synthetic WCTH projections (including the scaling of the variability to match the MISR observed WCTH variability).

In **Figure 8**, the left panels show the average rate of increase of each AMIP WCTH projection from 2001 to 2045, and the right panels show the estimated TOE (based on both the slope and  $\Delta$ mean statistics showing positive change in CTH with 95% confidence). The rate of increase and TOE are plotted against the ECS (top panels), TCR (middle panels), and global mean surface temperature (bottom panel, calculated as the difference between the 2035-2050 average and the 2001-2015 average) for each model. Data from all five latitude bands are plotted together and denoted by the different symbols (legend shown in top left panel), and each model corresponds to a different symbol color (legend shown in middle left panel).

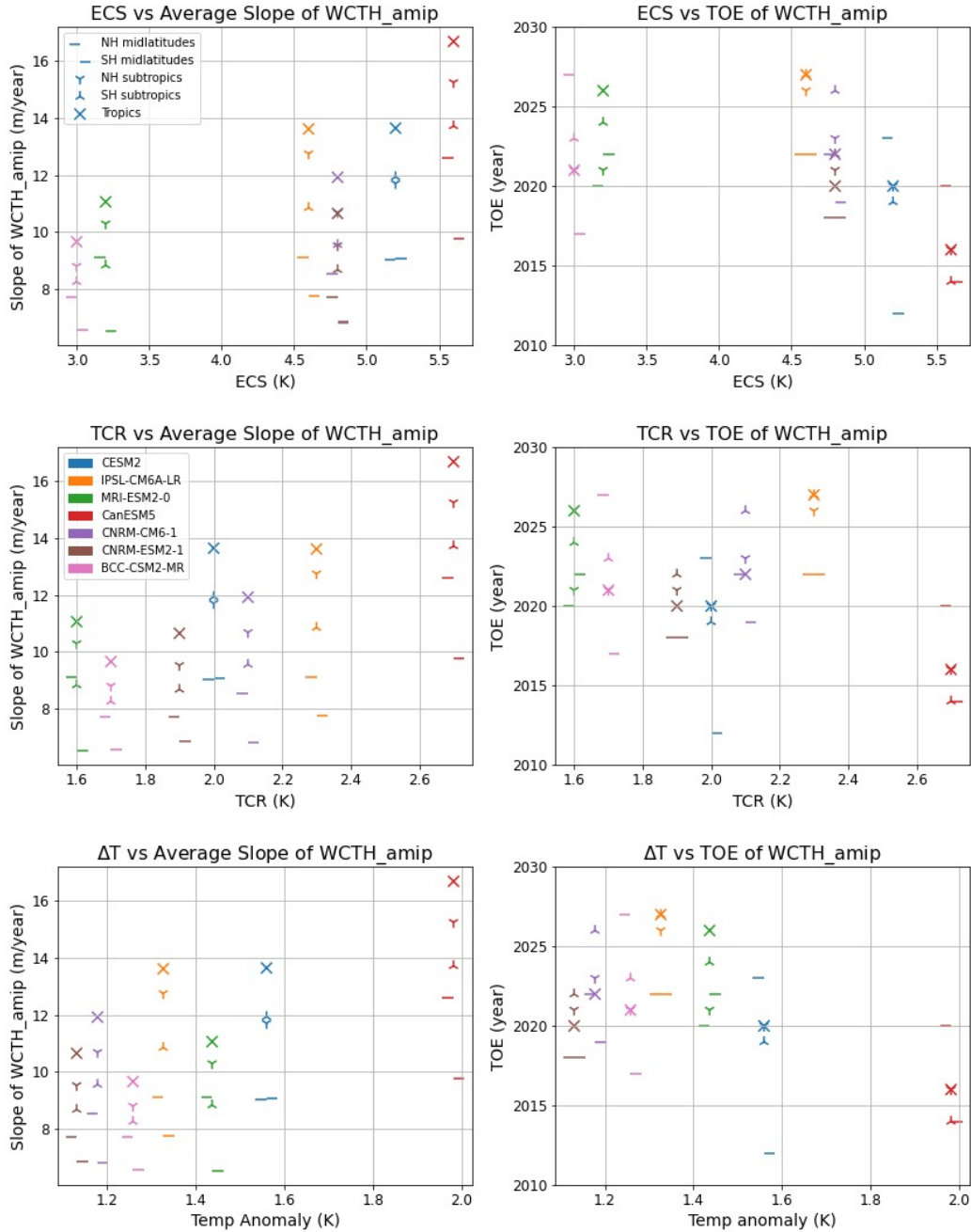
The results shown in the left panels of **Figure 8** indicate that in almost all seven of the models and by all three metrics, the average rate of increase in CTH (which in this analysis is synonymous with the rate of temperature increase in the upper troposphere) is fastest in the tropics and slowest in the SH midlatitudes. However as noted earlier, the amount of variance in CTH differs appreciably with latitude and the fast change in the tropics does not always lead to the earliest TOE. In fact, most models show the earliest TOE occurs for the SH midlatitudes with considerable variability regarding which latitude zone will have the latest TOE.

As regards the relationship between warming rate and TOE, the CanESM5 model has the strongest warming by all three metrics and the earliest TOE; while the MRI-ESM2-0 and BCC-CSM2-MR models that have the lowest ECS and TCR values, also have some of the latest TOE. Overall, we can conclude that while there is a clear tendency for the models with faster warming to have larger trends in CTH (left panels), this does not necessarily lead to earlier TOE (right

618 panels), and there does not appear to be a clear relationship between ECS, TCR or surface  $\Delta T$   
619 with TOE. Nonetheless these results suggest that the TOE estimates presented in Section 3 could  
620 occur by as much as 5 years later (roughly 2030), given the model spread.

621 As a reminder, we stress that the results in **Figure 8** are for the FAT-like increase which is  
622 faster than the true change in CTH, and the TOE shown here is expected to be earlier than the  
623 true TOE would be (because true CTH will increase more slowly than FAT) and these results  
624 may not capture regional differences accurately (since latitudinal deviations from FAT are  
625 possible if not likely). Rather the point of this analysis is only to investigate the spread in TOE  
626 values one might get from a larger ensemble of models and to investigate the potential for delay  
627 in TOE that we might expect from models that warm more slowly than CESM2 and IPSL.

628



629  
630  
631  
632  
633

**Figure 8** Rate of change of AMIP WCTH is plotted against the Equilibrium Climate Sensitivity (ECS), Transient Climate Response (TCR), and temperature anomaly in the left panels. All five latitude bands considered are plotted together, but color-coded. The right panels show the results of the TOE calculation plotted against ECS, TCR and Temperature anomaly

## 6. Discussion and Conclusions

634  
635

636 In a warming climate, the FAT and related PHAT hypotheses predict that the altitude or  
637 height of anvil detrainment and high-altitude clouds will increase following the height of a nearly  
638 constant temperature level, which creates a positive climate feedback. Climate models (nearly  
639 without exception) predict an increase in high cloud altitude, but the rate of increase varies  
640 between models. The satellite record to date provides little evidence of a global increase, which  
641 is unsurprising because of the small magnitude of the change relative to internal variability. In  
642 this study we use output from several CMIP6 models to determine when measurements by the  
643 NASA MISR instrument (which determines cloud-top-height using a stereo-imaging technique)  
644 might be expected to detect an upward trend in high cloud altitude. The model simulations  
645 employ a MISR simulator which produces histograms of cloud-top-height and optical depth  
646 consistent with those obtained from the MISR instrument, and a scheme was developed to  
647 calculate a weighted cloud-top-height (WCTH) metric for high clouds based on the histogram  
648 data. This metric, in combination with  $\Delta$ mean and slope statistics, and bootstrap resampling is  
649 used to determine a Time of Emergence (TOE) for the detection of change in WCTH with 95%  
650 confidence (in both statistics). The models were found to often underestimate variability in the  
651 MISR observation over the time period of the current observational record, and the model  
652 variability was scaled to match that found in the MISR data over the current observational record  
653 in the analysis.

654 The TOE analysis is performed using two CMIP6 models: CESM2 and IPSL-CM6A-LR,  
655 both of which generated MISR simulator output while running the ScenarioMIP SSP 585  
656 experiment. Both models predict that MISR will be capable of observing a trend in CTH  
657 sometime in the next 5 years (by 2024) in tropical, subtropical and mid-latitude zonal means of  
658 both hemispheres, and the models predict that in the Southern Hemisphere (SH) MISR should  
659 already have been capable of detecting trend in CTH. In fact, the MISR observations do show an  
660 increase (a positive trend) in the zonal mean WCTH in the SH midlatitudes (40° to 60° S) and a  
661 nearly significant change (just below the 95% level of confidence) for the SH subtropics.  
662 However, it is not clear that the observed SH trend is due to climate change rather than due to  
663 variations with ENSO and the Southern Annular Mode (SAM). Geiss and Marchand (2019) have  
664 shown that regional-scale variation in cloud amounts in the MISR CTH-OD histograms in the  
665 SH midlatitudes are dominated by variations that are strongly correlated with ENSO and SAM.  
666 Arguably, trends need to be confirmed in the Northern Hemisphere to firmly establish a global  
667 change in CTH is occurring.

668 The earlier detection in the SH is a result of the lower internal variability in the zonal mean  
669 WCTH in the SH. If anything, the models suggest that the upward trend in WCTH will be  
670 smaller in the SH than the NH (see left panels of **Figure 8**). The MISR observations and this  
671 analysis are restricted to ocean, and the lower variability over SH ocean is largely (but not  
672 entirely) due to the fact that there is more ocean (and hence more averaging in the zonal mean) in  
673 the southern hemisphere. IPSL does seem to capture the hemispheric asymmetry of WCTH  
674 variability reasonably well (even though it has persistently lower overall variability than  
675 observations). CESM2 does not appear to capture the hemispheric differences in the WCTH. In  
676 general, the models do not capture well the variability in WCTH observed by MISR, and the  
677 model output was scaled to match the observed variability in the TOE analysis.

678 A major assumption in the present work is that biases in the climatological base state of the  
679 models, including biases in WCTH, are not important for the assessment of trend detection.  
680 There are notable biases in the model simulated cloud occurrence histograms (which are detailed

681 in the supplementary materials). It is noteworthy that the apparent slope in WCTH is very similar  
682 between CESM2 and IPSL, and matches well the observations in at least the southern  
683 hemisphere (see bottom panels of **Figure 5**), in spite of the very different biases in the two  
684 models. Nonetheless, it remains an open area of study to determine if and how much differences  
685 in the base state of the models might influence the climate simulations, including the CTH  
686 trends.

687 Another important consideration is that CESM2 and IPSL-CM6A-LR are both rapidly  
688 warming models with high ECS and TCR in CMIP6 (Meehl et al., 2020), meaning the amount of  
689 surface warming for a doubling of CO<sub>2</sub> in the atmosphere is relatively large, and happens quickly  
690 compared with other models. It is logical to expect that models with lower ECS and TCR would  
691 have a later TOE. Based on analysis of feedback processes, the historical record, and the  
692 paleoclimate record Sherwood et al. (2020) estimate that the true ECS is likely lower than is  
693 produced by CESM2 and IPSL-CM6A-LR.

694 To investigate the dependence on ECS, we created synthetic MISR WCTH time series  
695 combining MISR output from AMIP simulations, with temperature data from SSP 585  
696 simulations (from models that performed the SSP 585 experiment, but did not produce MISR  
697 output for this run) and a Fixed-Anvil-Temperature assumption. In effect, the MISR simulated  
698 cloud profile found in the AMIP run remains fixed with temperature and shifts up to maintain the  
699 same mean temperature in the SSP 585 simulation. The synthetic WCTH projections showed that  
700 as expected, models that experience more warming also tend to have faster rising cloud tops.  
701 However this does not consistently lead to an earlier TOE. Rather, between the slower rate of  
702 increase in CTH in slower-warming models, and the spread in TOE between models with similar  
703 rates of warming, it is possible that a MISR detection of any trends in the Tropics or Northern  
704 Hemisphere CTH could be as much as 5 years further out than suggested by the analysis in  
705 Section 3.

706 Unfortunately, the TERRA satellite which houses the MISR instrument is running low on  
707 fuel and as of April 2021 the satellite has begun drifting from its fixed Equator Crossing Time  
708 (ECT). Diurnal variations in CTH will eventually cause an apparent change in CTH that is  
709 significant compared to that expected from climate change (shown in **Supplementary Figure**  
710 **S4**). When and how the orbit drifts will occur and how this will impact the ECT will have to be  
711 examined as part of future studies. Moving forward, NASA as part of the Aerosol, Cloud,  
712 Convection and Precipitation (ACCP) mission, plans to include a new stereo-imaging instrument  
713 which will make significantly more accurate measurements of cloud CTH than MISR. So, while  
714 there is likely to be a gap in the data record (and orbital differences will need to be considered  
715 carefully) there is hope that a long term, stereo-imaging, and calibration insensitive, data record  
716 on high cloud CTH will continue and will be able to constrain climate models. Even a continued  
717 negative signal in the tropics and NH (meaning non-detection of a change in CTH) should  
718 provide an upper bound on the possible rate of change.

## 719 **Acknowledgments**

720 This research was supported by the MISR project at the NASA Jet Propulsion Laboratory (under  
721 contract no. 1318945). We wish to acknowledge and thank the many modelling centers who  
722 contributed data to the Coupled Model Intercomparison Project that was necessary for this study,  
723 as well as Catherine Moroney, Steve Protack and everyone at NASA JPL and LaRC who  
724 produce the MISR CTH-OD data. The MISR CTH-OD data can be obtained from the NASA  
725 Langley Research Center Atmospheric Sciences Data

726 (DOI:10.5067/TERRA/MISR/MIL3MCOD.001). Additional details on obtaining observed and  
727 model simulated MISR CTH-OD datasets are given at the end of Section 2.

728

## 729 **References**

730

731 Aerenson, T. (2021). When Will MISR Detect Rising High Clouds? *Master of Science Thesis*  
732 *University of Washington*.

733 Bodas-Salcedo, A., Webb, M. J., Bony, S., Chepfer, H., Dufresne, J. L., Klein, S. A., ... John, V.  
734 O. (2011). COSP: Satellite simulation software for model assessment. *Bulletin of the*  
735 *American Meteorological Society*, 92(8), 1023–1043.  
736 <https://doi.org/10.1175/2011BAMS2856.1>

737 Bony, S., Stevens, B., Coppin, D., Becker, T., Reed, K. A., Voigt, A., & Medeiros, B. (2016).  
738 Thermodynamic control of anvil cloud amount. *Proceedings of the National Academy of*  
739 *Sciences of the United States of America*, 113(32), 8927–8932.  
740 <https://doi.org/10.1073/pnas.1601472113>

741 Boucher, O., Servonnat, J., Albright, A. L., Aumont, O., Balkanski, Y., Bastrikov, V., ...  
742 Vuichard, N. (2020). Presentation and Evaluation of the IPSL-CM6A-LR Climate Model.  
743 *Journal of Advances in Modeling Earth Systems*, 12(7), e2019MS002010.  
744 <https://doi.org/10.1029/2019MS002010>

745 Chepfer, H., Noel, V., Chiriaco, M., Wielicki, B., Winker, D., Loeb, N., & Wood, R. (2018). The  
746 Potential of a Multidecade Spaceborne Lidar Record to Constrain Cloud Feedback. *Journal*  
747 *of Geophysical Research: Atmospheres*, 123(10), 5433–5454.  
748 <https://doi.org/10.1002/2017JD027742>

749 Chepfer, H., Noel, V., Winker, D., & Chiriaco, M. (2014). Where and when will we observe  
750 cloud changes due to climate warming? *Geophysical Research Letters*, 41(23), 8387–8395.  
751 <https://doi.org/10.1002/2014GL061792>

752 Cho, E., Cho, M. J., & Eltinge, J. (2005). The Variance of Sample Variance for a Finite  
753 Population. *International Journal of Pure and Applied Mathematics*, 21(3), 387–394.  
754 Retrieved from [http://www.amstat.org/sections/srms/proceedings/y2004/files/Jsm2004-](http://www.amstat.org/sections/srms/proceedings/y2004/files/Jsm2004-000354.pdf)  
755 [000354.pdf](http://www.amstat.org/sections/srms/proceedings/y2004/files/Jsm2004-000354.pdf)

756 Danabasoglu, G., Lamarque, J. F., Bacmeister, J., Bailey, D. A., DuVivier, A. K., Edwards, J., ...  
757 Strand, W. G. (2020). The Community Earth System Model Version 2 (CESM2). *Journal of*  
758 *Advances in Modeling Earth Systems*, 12(2), e2019MS001916.  
759 <https://doi.org/10.1029/2019MS001916>

760 Diner, D. J., Beckert, J. C., Reilly, T. H., Bruegge, C. J., Conel, J. E., Kahn, R. A., ... Verstraete,  
761 M. M. (1998). Multi-angle imaging spectroradiometer (MISR) instrument description and  
762 experiment overview. *IEEE Transactions on Geoscience and Remote Sensing*, 36(4), 1072–  
763 1087. <https://doi.org/10.1109/36.700992>

764 Gates, W. L., Boyle, J. S., Covey, C., Dease, C. G., Doutriaux, C. M., Drach, R. S., ... Williams,  
765 D. N. (1999). An Overview of the Results of the Atmospheric Model Intercomparison  
766 Project (AMIP I). *Bulletin of the American Meteorological Society*, Vol. 80, pp. 29–55.  
767 [https://doi.org/10.1175/1520-0477\(1999\)080<0029:AOTRO>2.0.CO;2](https://doi.org/10.1175/1520-0477(1999)080<0029:AOTRO>2.0.CO;2)

768 Geiss, A., & Marchand, R. (2019). Cloud responses to climate variability over the extratropical  
769 oceans as observed by MISR and MODIS. *Atmospheric Chemistry and Physics*, 19(11),

- 7547–7565. <https://doi.org/10.5194/acp-19-7547-2019>
- 770 Hansen, J. (1984). Climate sensitivity: analysis of feedback mechanisms. *Climate Processes and*  
 771 *Climate Sensitivity*, 130–163. <https://doi.org/10.1029/GM029p0130>
- 772 Harrop, B. E., & Hartmann, D. L. (2012). Testing the role of radiation in determining tropical  
 773 cloud-top temperature. *Journal of Climate*, 25(17), 5731–5747.  
 774 <https://doi.org/10.1175/JCLI-D-11-00445.1>
- 775 Hartmann, D. L., & Larson, K. (2002). An important constraint on tropical cloud - climate  
 776 feedback. *Geophysical Research Letters*, 29(20), 12-1-12–14.  
 777 <https://doi.org/10.1029/2002gl015835>
- 778 Hillman, B. R., Marchand, R. T., Ackerman, T. P., Mace, G. G., & Benson, S. (2017). Assessing  
 779 the accuracy of MISR and MISR-simulated cloud top heights using CloudSat- and  
 780 CALIPSO-retrieved hydrometeor profiles. *Journal of Geophysical Research*, 122(5), 2878–  
 781 2897. <https://doi.org/10.1002/2016JD025510>
- 782 Hu, S., & Vallis, G. K. (2019). Meridional structure and future changes of tropopause height and  
 783 temperature. *Quarterly Journal of the Royal Meteorological Society*, 145(723), 2698–2717.  
 784 <https://doi.org/10.1002/qj.3587>
- 785 Jeevanjee, N., & Fueglistaler, S. (2020). Simple spectral models for atmospheric radiative  
 786 cooling. *Journal of the Atmospheric Sciences*, 77(2), 479–497. [https://doi.org/10.1175/JAS-](https://doi.org/10.1175/JAS-D-18-0347.1)  
 787 [D-18-0347.1](https://doi.org/10.1175/JAS-D-18-0347.1)
- 788 Kuang, Z., & Hartmann, D. L. (2007). Testing the fixed anvil temperature hypothesis in a cloud-  
 789 resolving model. *Journal of Climate*, 20(10), 2051–2057.  
 790 <https://doi.org/10.1175/JCLI4124.1>
- 791 Marchand, R. (2013). Trends in ISCCP, MISR, and MODIS cloud-top-height and optical-depth  
 792 histograms. *Journal of Geophysical Research Atmospheres*, 118(4), 1941–1949.  
 793 <https://doi.org/10.1002/jgrd.50207>
- 794 Marchand, R., & Ackerman, T. (2010). An analysis of cloud cover in multiscale modeling  
 795 framework global climate model simulations using 4 and 1 km horizontal grids. *Journal of*  
 796 *Geophysical Research Atmospheres*, 115(16), D16207.  
 797 <https://doi.org/10.1029/2009JD013423>
- 798 Marchand, R., Ackerman, T., Smyth, M., & Rossow, W. B. (2010). A review of cloud top height  
 799 and optical depth histograms from MISR, ISCCP, and MODIS. *Journal of Geophysical*  
 800 *Research Atmospheres*, 115(16), D16206. <https://doi.org/10.1029/2009JD013422>
- 801 Marchand, R. T., Ackerman, T. P., & Moroney, C. (2007). An assessment of Multiangle Imaging  
 802 Spectroradiometer (MISR) stereo-derived cloud top heights and cloud top winds using  
 803 ground-based radar, lidar, and microwave radiometers. *Journal of Geophysical Research*  
 804 *Atmospheres*, 112(6), D06204. <https://doi.org/10.1029/2006JD007091>
- 805 Meehl, G. A., Senior, C. A., Eyring, V., Flato, G., Lamarque, J. F., Stouffer, R. J., ... Schlund,  
 806 M. (2020). Context for interpreting equilibrium climate sensitivity and transient climate  
 807 response from the CMIP6 Earth system models. *Science Advances*, Vol. 6.  
 808 <https://doi.org/10.1126/sciadv.aba1981>
- 809 Moroney, C., Davies, R., & Muller, J. P. (2002). Operational retrieval of cloud-top heights using  
 810 MISR data. *IEEE Transactions on Geoscience and Remote Sensing*, 40(7), 1532–1540.  
 811 <https://doi.org/10.1109/TGRS.2002.801150>
- 812 Norris, J. R., Allen, R. J., Evan, A. T., Zelinka, M. D., O'Dell, C. W., & Klein, S. A. (2016).  
 813 Evidence for climate change in the satellite cloud record. *Nature*, 536(7614), 72–75.  
 814 <https://doi.org/10.1038/nature18273>
- 815

- 816 O'Neill, B. C., Tebaldi, C., Van Vuuren, D. P., Eyring, V., Friedlingstein, P., Hurtt, G., ...  
 817 Sanderson, B. M. (2016). The Scenario Model Intercomparison Project (ScenarioMIP) for  
 818 CMIP6. *Geoscientific Model Development*, 9(9), 3461–3482. [https://doi.org/10.5194/gmd-](https://doi.org/10.5194/gmd-9-3461-2016)  
 819 [9-3461-2016](https://doi.org/10.5194/gmd-9-3461-2016)
- 820 Rossow, W. B., Walker, A. W., & Garder, L. C. (1993). Comparison of ISCCP and other cloud  
 821 amounts. *Journal of Climate*, 6(12), 2394–2418. [https://doi.org/10.1175/1520-](https://doi.org/10.1175/1520-0442(1993)006<2394:COIAOC>2.0.CO;2)  
 822 [0442\(1993\)006<2394:COIAOC>2.0.CO;2](https://doi.org/10.1175/1520-0442(1993)006<2394:COIAOC>2.0.CO;2)
- 823 Schneider, S. H. (1972). Cloudiness as a Global Climatic Feedback Mechanism: The Effects on  
 824 the Radiation Balance and Surface Temperature of Variations in Cloudiness. *Journal of the*  
 825 *Atmospheric Sciences*, 29(8), 1413–1422. [https://doi.org/10.1175/1520-](https://doi.org/10.1175/1520-0469(1972)029<1413:caagcf>2.0.co;2)  
 826 [0469\(1972\)029<1413:caagcf>2.0.co;2](https://doi.org/10.1175/1520-0469(1972)029<1413:caagcf>2.0.co;2)
- 827 Seeley, J. T., Jeevanjee, N., & Romps, D. M. (2019). FAT or FiTT: Are Anvil Clouds or the  
 828 Tropopause Temperature Invariant? *Geophysical Research Letters*, 46(3), 1842–1850.  
 829 <https://doi.org/10.1029/2018GL080096>
- 830 Séférian, R., Nabat, P., Michou, M., Saint-Martin, D., Voldoire, A., Colin, J., ... Madec, G.  
 831 (2019). Evaluation of CNRM Earth System Model, CNRM-ESM2-1: Role of Earth System  
 832 Processes in Present-Day and Future Climate. *Journal of Advances in Modeling Earth*  
 833 *Systems*, 11(12), 4182–4227. <https://doi.org/10.1029/2019MS001791>
- 834 Sherwood, S. C., Webb, M. J., Annan, J. D., Armour, K. C., Forster, P. M., Hargreaves, J. C., ...  
 835 Zelinka, M. D. (2020, December 25). An Assessment of Earth's Climate Sensitivity Using  
 836 Multiple Lines of Evidence. *Reviews of Geophysics*, Vol. 58.  
 837 <https://doi.org/10.1029/2019RG000678>
- 838 Soden, B. J., & Held, I. M. (2006). An assessment of climate feedbacks in coupled ocean-  
 839 atmosphere models. *Journal of Climate*, 19(14), 3354–3360.  
 840 <https://doi.org/10.1175/JCLI3799.1>
- 841 Stephens, G. L. (2005, January 15). Cloud feedbacks in the climate system: A critical review.  
 842 *Journal of Climate*, Vol. 18, pp. 237–273. <https://doi.org/10.1175/JCLI-3243.1>
- 843 Swales, D. J., Pincus, R., & Bodas-Salcedo, A. (2018). The Cloud Feedback Model  
 844 Intercomparison Project Observational Simulator Package: Version 2. *Geoscientific Model*  
 845 *Development*, 11(1), 77–81. <https://doi.org/10.5194/gmd-11-77-2018>
- 846 Swart, N. C., Cole, J. N. S., Kharin, V. V., Lazare, M., Scinocca, J. F., Gillett, N. P., ... Winter,  
 847 B. (2019). The Canadian Earth System Model version 5 (CanESM5.0.3). *Geoscientific*  
 848 *Model Development*, 12(11), 4823–4873. <https://doi.org/10.5194/gmd-12-4823-2019>
- 849 Takahashi, H., Lebsock, M. D., Richardson, M., Marchand, R., & Kay, J. E. (2019). When Will  
 850 Spaceborne Cloud Radar Detect Upward Shifts in Cloud Heights? *Journal of Geophysical*  
 851 *Research: Atmospheres*. <https://doi.org/10.1029/2018JD030242>
- 852 Thompson, D. W. J., Bony, S., & Li, Y. (2017). Thermodynamic constraint on the depth of the  
 853 global tropospheric circulation. *Proceedings of the National Academy of Sciences of the*  
 854 *United States of America*, 114(31), 8181–8186. <https://doi.org/10.1073/pnas.1620493114>
- 855 Vallis, G. K., Zurita-Gotor, P., Cairns, C., & Kidston, J. (2015). Response of the large-scale  
 856 structure of the atmosphere to global warming. *Quarterly Journal of the Royal*  
 857 *Meteorological Society*, 141(690), 1479–1501. <https://doi.org/10.1002/qj.2456>
- 858 Voldoire, A., Saint-Martin, D., Sénési, S., Decharme, B., Alias, A., Chevallier, M., ... Waldman,  
 859 R. (2019). Evaluation of CMIP6 DECK Experiments With CNRM-CM6-1. *Journal of*  
 860 *Advances in Modeling Earth Systems*, 11(7), 2177–2213.  
 861 <https://doi.org/10.1029/2019MS001683>

- 862 Webb, M. J., Andrews, T., Bodas-Salcedo, A., Bony, S., Bretherton, C. S., Chadwick, R., ...  
863 Watanabe, M. (2017). The Cloud Feedback Model Intercomparison Project (CFMIP)  
864 contribution to CMIP6. *Geoscientific Model Development*, *10*(1), 359–384.  
865 <https://doi.org/10.5194/gmd-10-359-2017>
- 866 Wetherald, R. T., & Manabe, S. (1988). Cloud feedback processes in a general circulation model.  
867 *Journal of the Atmospheric Sciences*, *45*(8), 1397–1415. [https://doi.org/10.1175/1520-](https://doi.org/10.1175/1520-0469(1988)045<1397:CFPIAG>2.0.CO;2)  
868 [0469\(1988\)045<1397:CFPIAG>2.0.CO;2](https://doi.org/10.1175/1520-0469(1988)045<1397:CFPIAG>2.0.CO;2)
- 869 Wilks, D. S. (1997). Resampling hypothesis tests for autocorrelated fields. *Journal of Climate*,  
870 *10*(1), 65–82. [https://doi.org/10.1175/1520-0442\(1997\)010<0065:RHTFAF>2.0.CO;2](https://doi.org/10.1175/1520-0442(1997)010<0065:RHTFAF>2.0.CO;2)
- 871 Wu, T., Lu, Y., Fang, Y., Xin, X., Li, L., Li, W., ... Liu, X. (2019). The Beijing Climate Center  
872 Climate System Model (BCC-CSM): The main progress from CMIP5 to CMIP6.  
873 *Geoscientific Model Development*, *12*(4), 1573–1600. [https://doi.org/10.5194/gmd-12-1573-](https://doi.org/10.5194/gmd-12-1573-2019)  
874 [2019](https://doi.org/10.5194/gmd-12-1573-2019)
- 875 Yukimoto, S., Kawai, H., Koshiro, T., Oshima, N., Yoshida, K., Urakawa, S., ... Ishii, M.  
876 (2019). The meteorological research institute Earth system model version 2.0, MRI-  
877 ESM2.0: Description and basic evaluation of the physical component. *Journal of the*  
878 *Meteorological Society of Japan*, *97*(5), 931–965. <https://doi.org/10.2151/jmsj.2019-051>
- 879 Zelinka, M. D., & Hartmann, D. L. (2010). Why is longwave cloud feedback positive? *Journal*  
880 *of Geophysical Research Atmospheres*, *115*(16). <https://doi.org/10.1029/2010JD013817>
- 881 Zelinka, M. D., Klein, S. A., Taylor, K. E., Andrews, T., Webb, M. J., Gregory, J. M., & Forster,  
882 P. M. (2013). Contributions of different cloud types to feedbacks and rapid adjustments in  
883 CMIP5. *Journal of Climate*, *26*(14), 5007–5027. [https://doi.org/10.1175/JCLI-D-12-](https://doi.org/10.1175/JCLI-D-12-00555.1)  
884 [00555.1](https://doi.org/10.1175/JCLI-D-12-00555.1)
- 885 Zelinka, M. D., Myers, T. A., McCoy, D. T., Po-Chedley, S., Caldwell, P. M., Ceppi, P., ...  
886 Taylor, K. E. (2020). Causes of Higher Climate Sensitivity in CMIP6 Models. *Geophysical*  
887 *Research Letters*, *47*(1). <https://doi.org/10.1029/2019GL085782>
- 888 Zhou, C., Dessler, A. E., Zelinka, M. D., Yang, P., & Wang, T. (2014). Cirrus feedback on  
889 interannual climate fluctuations. *Geophysical Research Letters*, *41*(24), 9166–9173.  
890 <https://doi.org/10.1002/2014GL062095>  
891